







A White Dwarf-Main Sequence Binary Unveiled by Time-Domain Observations from LAMOST and TESS

LING-LIN ZHENG ¹, WEI-MIN GU ¹, MOUYUAN SUN ¹, ZHIXIANG ZHANG ¹, TUAN YI ¹, JIANFENG WU ¹,
JUNFENG WANG ¹, JIN-BO FU ¹, SEN-YU QI ¹, FAN YANG ², SONG WANG ³, LIANG WANG ^{4,5}, ZHONGRUI BAI,³
HAOTONG ZHANG ³, CHUN-QIAN LI ³, JIAN-RONG SHI ³, WEIKAI ZONG ², YU BAI ³, AND JIFENG LIU ^{3,6}

¹Department of Astronomy, Xiamen University, Xiamen, Fujian 361005, P. R. China

²Department of Astronomy, Beijing Normal University, Beijing 100875, China

³National Astronomical Observatories, Chinese Academy of Sciences, Beijing 100101, China

⁴Nanjing Institute of Astronomical Optics & Technology, Chinese Academy of Sciences, Nanjing 210042, China

⁵CAS Key Laboratory of Astronomical Optics & Technology, Nanjing Institute of Astronomical Optics & Technology, Chinese Academy of Sciences, Nanjing 210042, China

⁶College of Astronomy and Space Science, University of Chinese Academy of Sciences, Beijing 100049, China

ABSTRACT

We report a single-lined white dwarf-main sequence binary system, LAMOST J172900.17+652952.8, which is discovered by LAMOST’s medium resolution time-domain surveys. The radial velocity semi-amplitude and orbital period of the optical visible star are measured by using the Palomar 200-inch telescope follow-up observations and the light curves from *TESS*. Thus the mass function of the invisible candidate white dwarf is derived, $f(M_2) = 0.120 \pm 0.003 M_\odot$. The mass of the visible star is measured based on the spectral energy distribution fitting, $M_1 = 0.81^{+0.07}_{-0.06} M_\odot$. Hence, the mass of its invisible companion is $M_2 \gtrsim 0.63 M_\odot$. The companion ought to be a compact object rather than a main-sequence star owing to the mass ratio $q = M_2/M_1 \gtrsim 0.78$ and the single-lined spectra. The compact object is likely to be a white dwarf except for small inclination angle, $i \lesssim 40^\circ$. By using the GALEX NUV flux, the effective temperature of the white dwarf candidate is constrained as $T_{\text{eff}}^{\text{WD}} \lesssim 12000 - 13500$ K. It is difficult to detect white dwarfs which are outshone by their bright companions via single-epoch optical spectroscopic surveys. Therefore, the optical time-domain surveys can play an important role in unveiling invisible white dwarfs and other compact objects in binaries.

Keywords: Close binary stars (254) — Light curves (918) — Radial velocity (1332) — White dwarf stars (1799)

1. INTRODUCTION

A white dwarf-main sequence (WD-MS) binary is a system composed of a WD and a main-sequence star. The study of WDs can facilitate us to understand the physical properties of binaries and the evolution of the Milky Way (e.g., Ren et al. 2018). If the separation of two stars is far enough ($\gtrsim 10$ AU) that they can evolve separately, the more massive one ($\lesssim 10 M_\odot$) will reach the end of its life as a WD earlier than its less massive companion (e.g., Rebassa-Mansergas et al. 2021). The stellar evolution model predicts that more than 97% of the stars with masses $\lesssim 10 M_\odot$ in our Galaxy eventually form as WDs (e.g., García-Berro et al. 1997; Fontaine et al. 2001; Taani 2017; Kepler et al. 2019).

The unique characteristics of WDs, such as the blue colors and relatively large proper motions, have traditionally been used to identify WDs (e.g., Raddi et al. 2017). Over the past decades, optical telescopes with high-resolution, high-precision, and wide-field, have led to a significant increase in the sample size of WD-MS binaries (e.g., Silvestri et al. 2006; Heller et al. 2009; Liu et al. 2012; Li et al. 2014; Cojocaru et al. 2017; Bar et al. 2017; Ren et al. 2018). Most of these binaries are identified by the prominent lines of WDs shown in the spectra, e.g., Balmer lines in the

blue spectra for the hot WDs (the effective temperature $\gtrsim 15000$ K, Wesseliuss & Koester 1978). However, due to the faint nature of WDs, the search methods relying on the spectral components of WDs are often limited to nearby sources (e.g., Bar et al. 2017; Kilic et al. 2020; Rebassa-Mansergas et al. 2021). The Sloan Digital Sky Survey (SDSS) found a large WD sample including hot WDs (e.g., Rebassa-Mansergas et al. 2016). Such hot WDs are sometimes indistinguishable from quasars in color space. Hence, a large fraction of the identified and known WD-MS binaries in SDSS are composed of relatively cool WDs with late-type companions (Rebassa-Mansergas et al. 2012; Ren et al. 2018; Rebassa-Mansergas et al. 2021). Motivated by complementing the sample of WDs with bright companions (e.g., F, G, and K type star), some research attempt to select the sources based on the conditions of UV excess and the stellar temperature (e.g., Maxted et al. 2009; Parsons et al. 2016; Rebassa-Mansergas et al. 2017; Hernandez et al. 2021) or the multi-band photometry (e.g., Maxted et al. 2009).

The superiority of optical time-domain surveys, including spectroscopy and photometry, allow us to make continuous tracking of the observed targets over time. We can derive the semi-amplitude K of radial velocity V_r and photometric variation period T_{ph} of a binary system from time-domain surveys. The time-domain method has the potential to unveil distant faint WDs, and enlarge the sample of WDs with bright companions (e.g., A, F, G, and K type star) even without the necessary characteristics (e.g., UV excess or blue color).

A multi-object time-domain spectroscopic survey would be vital for constraining K (or even T_{ph}) for a tremendous amount of binaries. LAMOST (Large Sky Area Multi-Object fiber Spectroscopic Telescope)¹ is an optical ground-based telescope with wide-field of view ($\sim 5^\circ$) and a large number of fibers ~ 4000 (Cui et al. 2012; Zhao et al. 2012; Liu et al. 2020; Zong et al. 2018, 2020). Not only does it provide us with a huge number of stellar spectra, but also it allows for multiple observations of the same target. Notably, the LAMOST medium-resolution survey (hereafter MRS, whose spectral resolution $R \sim 7500$, $G \lesssim 15$ mag) will complete about 60 high-quality spectroscopic observations for each of 200,000 sources ($G \sim 14$ mag) within five years (2018-2023; Liu et al. 2020). This time-domain survey will be of great help to our search for compact binaries, including binaries with WDs, neutron stars (NS), or black holes (e.g., Yi et al. 2019). Up to the Data Release 8 (DR8), LAMOST has released more than 10 million stellar spectra², and it has some fruitful results in the search for compact binaries or candidates (e.g., Gu et al. 2019; Liu et al. 2019; Zheng et al. 2019; Wiktorowicz et al. 2020; Yang et al. 2021; Zhang et al. 2022).

For sources with multiple spectroscopic observations from LAMOST, *TESS* (Transiting Exoplanet Survey Satellite)³ survey can serve as a perfect complement in photometry. *TESS* is an all-sky survey spacecraft to collect the photometric data for exoplanets transiting bright and nearby stars (Ricker et al. 2015), and its detection limit is about 15 *TESS* magnitude. *TESS* performs both 2-minute and 30-minute cadence observations (Stassun et al. 2018). Hence, the *TESS* observations are vital for probing short-period binaries.

The joint effort of LAMOST and *TESS* has great potential for hunting for short-period binaries that host compact objects. Mu et al. (2022) presents a sample of compact object candidates with K/M-dwarf companions by using radial velocities from LAMOST and the photometric period from *TESS*. Here we report the discovery of a new object LAMOST, J172900.17+652952.8 (hereafter J1729+6529), which is a WD-MS binary system with a bright K-type companion discovered by radial velocities and periodic light curves. The object has Palomar 200-inch telescope (P200) follow-up observations, as well as 20 sectors of *TESS* observations (each sector is 27.4 days long).

We organize the paper as follows. The observations and data reduction are presented in Section 2. Results are described in Section 3. In Section 4, we discuss the implications of our results.

2. OBSERVATIONS AND DATA REDUCTION

2.1. The discovery of J1729+6529

J1729+6529 is a single-lined object selected from the medium-resolution survey of LAMOST DR7, whose equatorial coordinate is R.A. = 262.25073° and Decl. = $+65.49800^\circ$ in J2000. This source draws our attention for the rapid variation of radial velocity, i.e., $|\Delta V_r| > 100$ km s⁻¹ within 141 minutes. We judge the spectra of the source are single-lined by using the cross correlation functions (CCFs; refer Merle et al. 2017; Li et al. 2021).

We collect the photometric data of J1729+6529 from different sky surveys, including *TESS*, ASAS-SN, and ZTF. We search the MIKULSKI ARCHIVE FOR SPACE TELESCOPES (MAST)⁴ with a maximum searching radius of

¹ <http://www.lamost.org/public/?locale=en>

² <http://www.lamost.org/dr8/v1.1/>

³ <https://tess.mit.edu/>

⁴ <https://mast.stsci.edu/portal/Mashup/Clients/Mast/Portal.html>

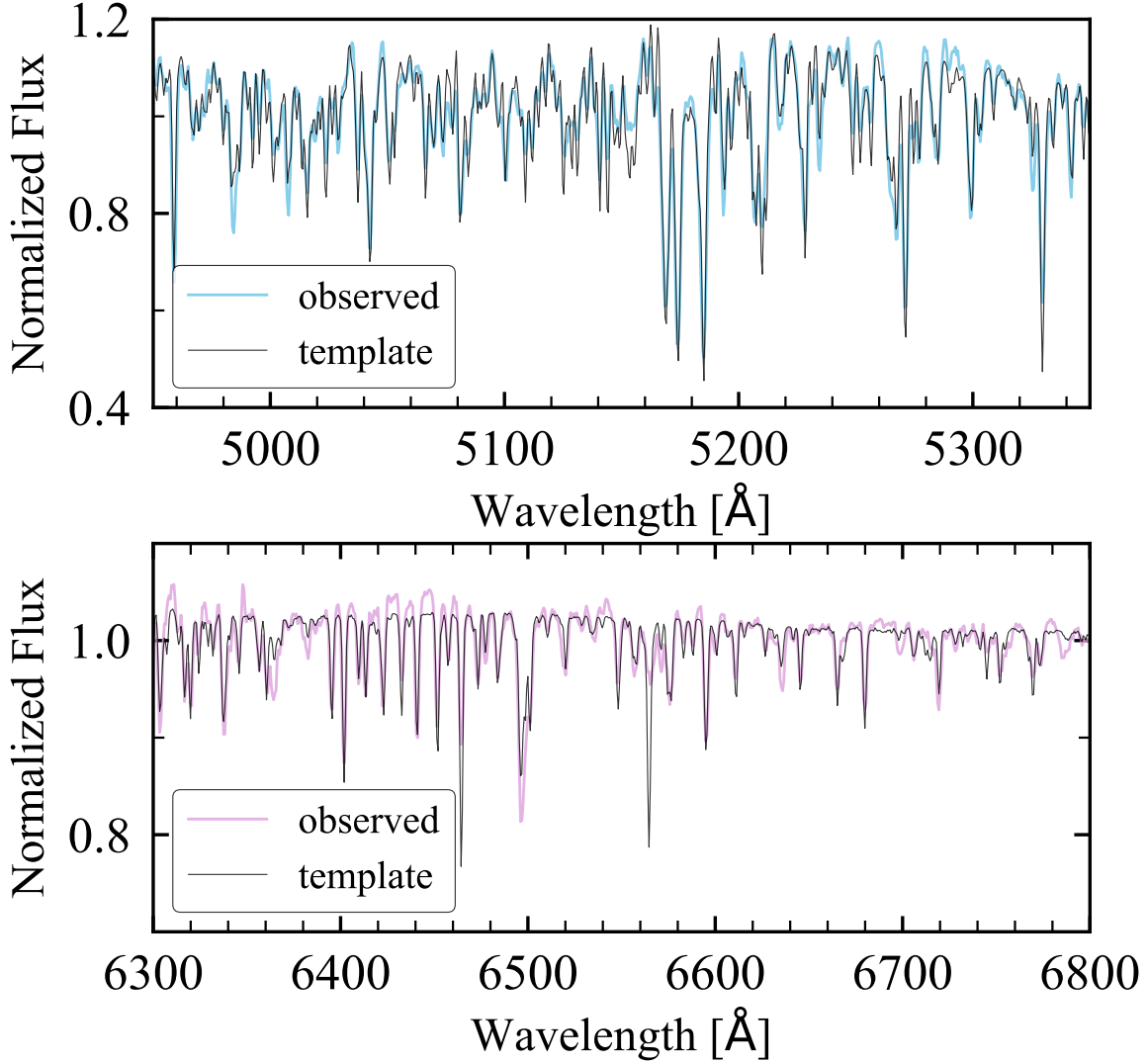


Figure 1. The LAMOST coadd spectrum (blue and pink curves) of J1729+6529 and the best-matching template (black curves). The upper and lower panels are for the blue and red arms, respectively.

0.5'', and found that our target has 20 sectors of *TESS* observations. We derive the processed light-curve data of the sectors for 14-19, 21-22, and 24-26 directly from the MAST. Then fold the photometric data according to the period revealed by the Lomb-Scargle algorithm, which is a method by means of the Fourier transform to extract periodic signals in the non-uniform time domain (Lomb 1976; Scargle 1981). We find that all folded light curves show periodic signals.

Due to only several LAMOST V_r measurements for J1729+6529 on the same night, the semi-amplitude K cannot be constrained reliably. Hence, we implement the follow-up observations of J1729+6529 by using DBSP (Double Spectrograph) of P200 telescope (Oke & Gunn 1982) on June 12 and 24, 2020. The seeing is about 1.3'' during the observation. The spectral coverage is [4047.9 Å, 5594.9 Å] with a resolving power of 3415 for the blue-side, and [5788.4 Å, 7089.5 Å] with a resolving power of 4524 for the red-side.

We follow the standard procedures and use IRAF⁵ to extract the 1-D spectra. Then we reject the cosmic rays of the observed spectra by using the median filter, and all spectra are normalized by the Gaussian filter method. We use The_Payne (Ting et al. 2019) to interpolate the BT-Settl spectral grid, which is a spectral interpolate tool based on neural networks. To obtain the best matching template, we minimize the χ^2 of the template model and the observed

⁵ <https://github.com/joequant/iraf>

spectrum. The χ^2 is expressed as

$$\chi^2 = \sum_i \left(\frac{y_i - y_{\text{model}}}{\sigma_i} \right)^2, \quad (1)$$

where y_i is the spectral flux of the i -th point, and y_{model} is the spectral flux of the model. The best matching spectral template (see the black curves of Figure 1), which corresponds to the smallest value of the χ^2 , is selected by interpolating the grid from the BT-Settl model. Next, we use the cross-correlation function (CCF; Tonry & Davis 1979; Gaskell & Peterson 1987; Zverko et al. 2007) in the *spectool* package⁶ to measure V_r of LAMOST and P200 by cross-matching the template and the observed spectra. The blue and pink curves in Figure 1 are selected from LAMOST, shown as an example. V_r can be calculated by $V_r = c \Delta\lambda/\lambda = c \Delta\ln\lambda = c \Delta u$, where c is the speed of light, λ is the wavelength. The CCF is defined by the following equation:

$$\text{CCF}(\Delta u) = \int \frac{[f(u) - \bar{f}][T(u - \Delta u) - \bar{T}]}{\sigma_f \sigma_T} du, \quad (2)$$

where $f(u)$ and $T(u)$ are the observed and template spectra in log wave space; σ_f and σ_T are the standard deviations of the observed spectrum and the template, respectively. The sampling interval of the V_r is set as 1 km s^{-1} . Since the neon bulb (for the HeNeAr lamp) was broken during the P200 observation, we only take the blue-side of the P200 spectra to measure the corresponding V_r . The used wavelength windows in the measured process are $[5200 \text{ \AA}, 5350 \text{ \AA}]$ and $[5200 \text{ \AA}, 5500 \text{ \AA}]$ for the spectra of LAMOST and P200, respectively. The uncertainties of V_r are measured by using the ‘‘flux randomization/random subset sampling (FR/RSS)’’ method (Peterson et al. 1998), which is a Monte Carlo approach. For each Monte Carlo simulation, we add a random flux to each pixel based on the 1σ flux uncertainties of that pixel (i.e., the ‘‘FR’’ step), and randomly removes data points in the spectrum (i.e., the ‘‘RSS’’ step). We run the Monte Carlo simulation 1000 times to obtain the mock $V_{r,m}$. The uncertainty of V_r is the standard deviation of the distribution of $V_{r,m}$. V_r measurements are shown in Table 1.

2.2. The determination of the orbital period and the radial-velocity semi-amplitude

The photometric periods from *TESS*, ASAS-SN, and ZTF are all different. These three periods measured by the Lomb-Scargle algorithm are 0.6 days, 3 days and 1.2 days, respectively. We derive the true orbital period of J1729+6529 is 0.6 days by fitting the radial velocities, the details of which are discussed below.

The radial velocity fit for the visible star is conducted by using *The Joker*⁷ (Price-Whelan et al. 2017). The formula used for the fit is expressed as follows:

$$V_r(t) = v_0 + K[\cos(f + \omega) + e \cos(\omega)], \quad (3)$$

where v_0 , K , f , ω , and e represent the systemic velocity, the velocity semi-amplitude, the true anomaly, the argument of periastron, and eccentricity, respectively. The eccentricity is fixed to zero, and the calibration offset between instruments of LAMOST and P200 is set as a free parameter in the fitting process. The prior of the offset is assumed to follow the Gaussian distribution, whose mean value and standard deviation are 0 km s^{-1} and 5 km s^{-1} , respectively⁸. Due to our incomplete understanding of the radial-velocity uncertainties and the intrinsic radial-velocity scatter, there may exist a jitter in the radial-velocity curve (Price-Whelan et al. 2017). We consider this jitter s in the fitting, and the derived value is given in Table 2. The fitting results (see Table 2) suggest that models with periods of 3 days and 1.2 days cannot explain the observed V_r . In contrast, the model with the prior period from *TESS* shows a perfect fit to the radial velocities (see the third panel of Figure 2, from top to bottom). Thus we argue that the orbital period with its 1σ uncertainty is 0.600303(6) days (given by *The Joker*), which is consistent with the *TESS*’s photometric period 0.600149 days (the highest peak in the first panel of Figure 2). The third panel is the radial-velocity curve folded by the orbital period P_{orb} , and the corresponding semi-amplitude of the best-fitting radial-velocity curve (black curve) is $K = 124.4_{-1.1}^{+1.0} \text{ km s}^{-1}$. The fourth panel gives the residuals obtained by subtracting the theoretical V_r (Equation (3)) from that of the observed. The uncertainties of the residuals are calculated by $\sqrt{(V_{r,\text{err}})^2 + s^2}$, where $V_{r,\text{err}}$ is the uncertainty of the V_r .

⁶ <https://gitee.com/zzxihep/spectool>

⁷ <https://github.com/adrn/thejoker>

⁸ <https://thejoker.readthedocs.io/en/latest/examples/5-Calibration-offsets.html>

Table 1. Observation log of the V_r

Instrument	Median UTC (yyyy-mm-dd hh:mm:ss)	Phase	Exposure time (s)	V_r (km s ⁻¹)
LAMOST	2019-05-27 16:40:00	0.37	1200	-98.7 ± 1.7
	2019-05-27 17:04:00	0.40	1200	-81.9 ± 2.1
	2019-05-27 17:27:00	0.43	1200	-62.1 ± 1.7
	2019-05-27 17:51:00	0.46	1200	-44.4 ± 1.1
	2019-05-27 18:14:00	0.48	1200	-21.7 ± 1.2
	2019-05-27 18:38:00	0.51	1200	-2.9 ± 1.2
	2019-05-27 19:00:00	0.54	1053	16.9 ± 1.3
P200	2020-06-12 04:49:25	0.89	60	62.3 ± 3.4
	2020-06-12 04:59:30	0.90	600	54.3 ± 1.9
	2020-06-12 05:10:11	0.92	600	45.3 ± 1.9
	2020-06-12 05:20:33	0.93	600	37.6 ± 2.0
	2020-06-12 07:44:33	0.09	720	-84.6 ± 1.8
	2020-06-12 07:56:55	0.11	720	-93.6 ± 1.9
	2020-06-12 08:09:17	0.12	720	-105.6 ± 1.9
	2020-06-12 08:21:38	0.14	720	-113.4 ± 1.9
	2020-06-12 10:04:28	0.26	720	-137.3 ± 1.8
	2020-06-12 10:16:49	0.27	720	-135.5 ± 1.9
	2020-06-12 10:29:11	0.28	720	-133.5 ± 1.9
	2020-06-12 10:41:33	0.30	720	-132.5 ± 1.8
	2020-06-24 07:34:46	0.07	600	-71.0 ± 3.4
	2020-06-24 07:45:08	0.08	600	-80.8 ± 3.2
	2020-06-24 07:55:29	0.10	600	-87.8 ± 2.9

Notes. Instrument: the telescopes used for the observations of J1729+6529. Median UTC: the intermediate time between the start and the end of the observation.

Phase: the orbital phase.

Exposure time: duration of the observation.

V_r : the radial velocity measured by the CCF.

The first panel (i.e., the top one) in Figure 2 shows the power spectral density of the *TESS* light curve in sector 14. The light curve in the second panel is folded with the orbital period of 0.600303 days (i.e., folded by using the period from radial-velocity fitting); the folded light curve shows the ellipsoidal-like variations. We interpret it as a result of the tidal deformation of the visible star. The two peaks in the folded light curve have different heights, which may be caused by the stellar spots. The light curve and radial-velocity curve in Figure 2 are folded by using the same ephemeris, i.e., $T(\phi = 0) = 2458631.569431 \text{ HJD} + 0.600303 \times N$, where the phase $\phi = 0$ corresponds to the visible star in the superior conjunction, and HJD is the Heliocentric Julian Date. Light curves of all other sectors are folded by the same period of 0.6003 days; they also show periodic variations (see Section 3.4).

3. RESULTS

3.1. Mass function

The mass function (the minimum mass of the invisible star) can be calculated by the equation:

$$f(M_2) = \frac{(M_2 \sin i)^3}{(M_1 + M_2)^2} = \frac{K^3 P_{\text{orb}} (1 - e^2)^{3/2}}{2\pi G}, \quad (4)$$

where M_1 and M_2 are the masses of the visible star and its companion, i is the orbital inclination angle, e is the eccentricity (fixed to zero), and G is the gravitational constant. The calculated value is $f(M_2) = 0.120 \pm 0.003 M_\odot$.

3.2. Properties of the visible star

Table 2. *The Joker* fitting parameters

parameter	value and uncertainty
(1)	(2)
P_{orb} [days]	0.600303(6)
K [km s $^{-1}$]	$124.4^{+1.0}_{-1.1}$
v_0 [km s $^{-1}$]	$-9.6^{+4.0}_{-3.9}$
s [km s $^{-1}$]	$0.1^{+0.3}_{-0.1}$
dv_0 [km s $^{-1}$]	$-4.2^{+3.6}_{-3.5}$
ω [rad]	3.1 ± 2.0
$f(M_2)$ [M_{\odot}]	0.120 ± 0.003
e	fixed to 0
χ^2	19.4
N_{V_r}	22

Notes. P_{orb} : the orbital period.

K : the radial velocity semi-amplitude of the visible star.

v_0 : the systemic velocity.

s : the jitter of the radial-velocity curve.

dv_0 : the calibration offset between LAMOST and P200.

ω : the argument of periastron.

$f(M_2)$: the mass function.

e : the orbit eccentricity.

χ^2 : the Chi-square value of the radial-velocity fitting.

N_{V_r} : the number of radial velocities.

We derive the stellar parameters of the visible star by spectral energy distributing (SED) fitting. The fitting is made by using the Python tool, ARIADNE (spectrAl eneRgy dIstribution bAyesian moDel averagiNg fittEr; Vines & Jenkins 2022)⁹. We collect the photometric data in various bands from different sky surveys. The data from *GALEX* (Martin et al. 2005; Morrissey et al. 2007), SDSS (Abazajian et al. 2009), APASS (Henden et al. 2009, 2010), Pan-STARRS (Chambers et al. 2016; Magnier et al. 2020; Waters et al. 2020), *Gaia* (Gaia Collaboration et al. 2018), *TESS* (Stassun et al. 2019), 2MASS (Skrutskie et al. 2006), and ALLWISE (Cutri et al. 2021) are queried via the Vizier catalog¹⁰ with a maximum matching radius of 2'', and are taken as the input parameters to ARIADNE. The collected photometric data and the corresponding calculated flux are listed in Table 3. The two parameters, the parallax of 4.34 ± 0.02 mas from *Gaia* DR3 (Gaia Collaboration 2022) and the extinction value of $A_v = 0.09$ from Amôres et al. (2021) in the GALExtin¹¹ are fixed in our fit. Note that we implicitly assume that the observed SED is dominated by a single star (i.e., the visible star) since it is a single-lined system.

The SED fitting result is displayed in Figure 3. The green curve in Figure 3 is obtained by weighting the four stellar atmosphere models, which are Phoenix v2¹², BT-Models¹³, Castelli & Kurucz¹⁴, and Kurucz 1993¹⁵, and the corresponding weights are 0.24, 0.08, 0.59, and 0.09, as determined by the ARIADNE code. The black dots and gray circles in the upper panel each represent the observed and synthetic fluxes. The residuals (triangles in the lower panel of Figure 3) are defined as $(f_p - f_s)/f_s$, where f_p and f_s are the photometric and synthetic fluxes, respectively. The best-fitting parameters (see Figure 4) and their 1σ uncertainties are obtained from the MCMC chains; the results show the spectral type of the visible star is K2V, and the parameters are: $T_{\text{eff}} = 4896^{+19}_{-25}$ K, $\log g = 4.58 \pm 0.03$ dex, $[\text{Fe}/\text{H}] = -0.03^{+0.06}_{-0.08}$, radius $R_1 = 0.77 \pm 0.01 R_{\odot}$. The luminosity $L_1 = 4\pi R_1^2 \sigma T_{\text{eff}}^4 = 0.31^{+0.01}_{-0.02} L_{\odot}$. The radius and luminosity are statistically consistent with those from *Gaia* DR3: $R_1 = 0.810 \pm 0.004 R_{\odot}$ and $L_1 = 0.340 \pm 0.006 L_{\odot}$.

We calculate the mass of the visible star (M_1) by different methods to check their consistency. First, we take 10,000 samplings of $\log g$ and the corresponding radius from the ARIADNE's nested MCMC sampling, and derive

⁹ <https://github.com/jvines/astroARIADNE>

¹⁰ <https://vizier.u-strasbg.fr/viz-bin/VizieR-4>

¹¹ <http://www.galexin.org/>

¹² <ftp://phoenix.astro.physik.uni-goettingen.de/HiResFITS/PHOENIX-ACES-AGSS-COND-2011/>

¹³ <http://osubdd.ens-lyon.fr/phoenix/>

¹⁴ <http://ssb.stsci.edu/cdbs/tarfiles/synphot3.tar.gz>

¹⁵ <http://ssb.stsci.edu/cdbs/tarfiles/synphot4.tar.gz>

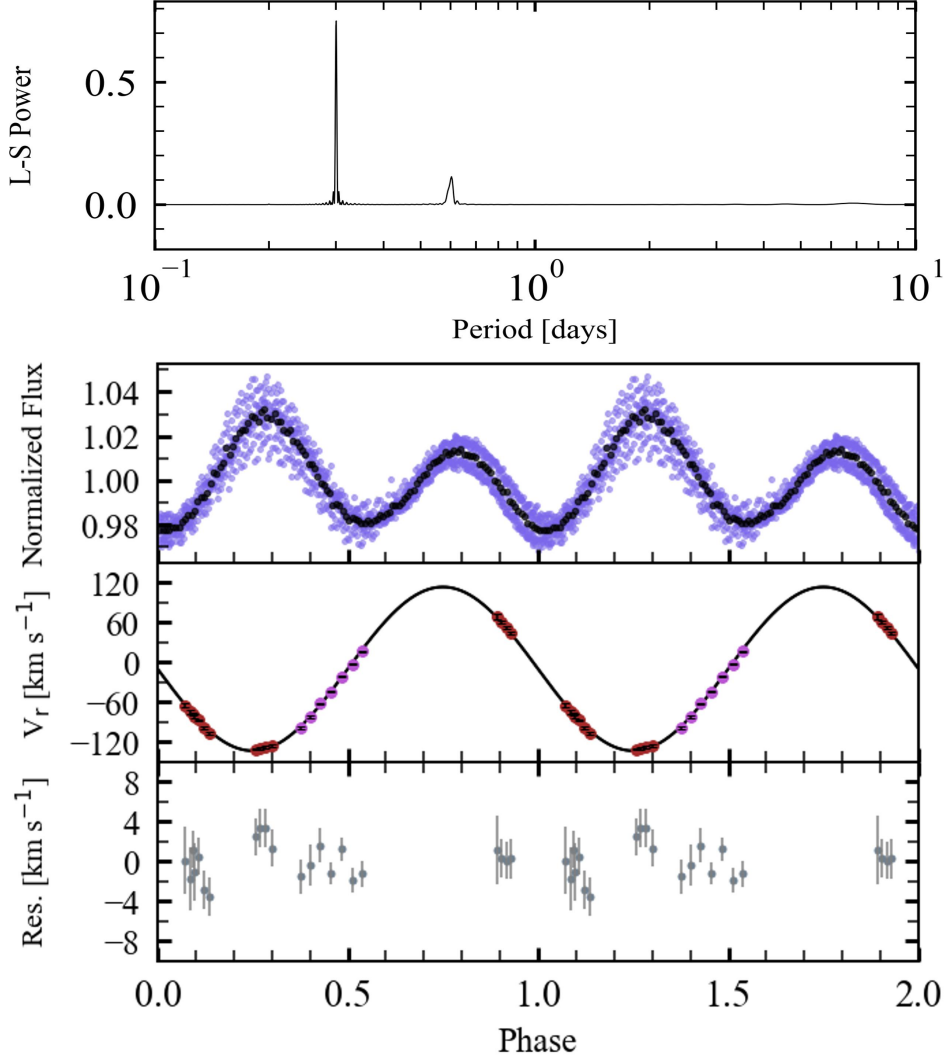


Figure 2. The first panel (from top to bottom) shows the Lomb-Scargle power peak. The second panel displays the *TESS* light curve folded with the orbital period of 0.600303 days. The black dots are binned over ten violet dots. The third panel is the radial velocities folded by the period of 0.600303 days. The black curve is the best-fitting radial-velocity curve with a semi-amplitude of $K = 124.4^{+1.0}_{-1.1} \text{ km s}^{-1}$. The pink dots represent the data collected from LAMOST, and the dark red dots are from P200. The errors of the photometric data are too small to be shown in the light curve, and the errors of the radial velocities are shown with the short bars over the dots (see the third panel). The residuals in the fourth panel are obtained by subtracting the observed radial velocities from the best fit model (Equation (3)). It should be noted that the eccentricity is fixed to zero when fitting the radial velocities.

the corresponding mass by $M_1 = gR_1^2 / G$. The median value and its uncertainties the 16th and 84th percentiles $M_1 = 0.81^{+0.07}_{-0.06} M_\odot$. Second, we refer to the mass-luminosity relation of Henry & McCarthy (1993) to calculate the mass M_1 from the infrared J, H, and K luminosity. The corresponding magnitude of the three bands are $11.516 \pm 0.022 \text{ mag}$, $11.004 \pm 0.021 \text{ mag}$, $10.889 \pm 0.019 \text{ mag}$ from 2MASS (Two Micron All Sky Survey)¹⁶. The derived masses of three bands are similar, i.e., $M_1^* = 0.79 \pm 0.1 M_\odot$, which is in accord with the mass calculated by the first method.

3.3. The nature of the invisible object: a compact object or a normal star?

¹⁶ <https://old.ipac.caltech.edu/2mass/>

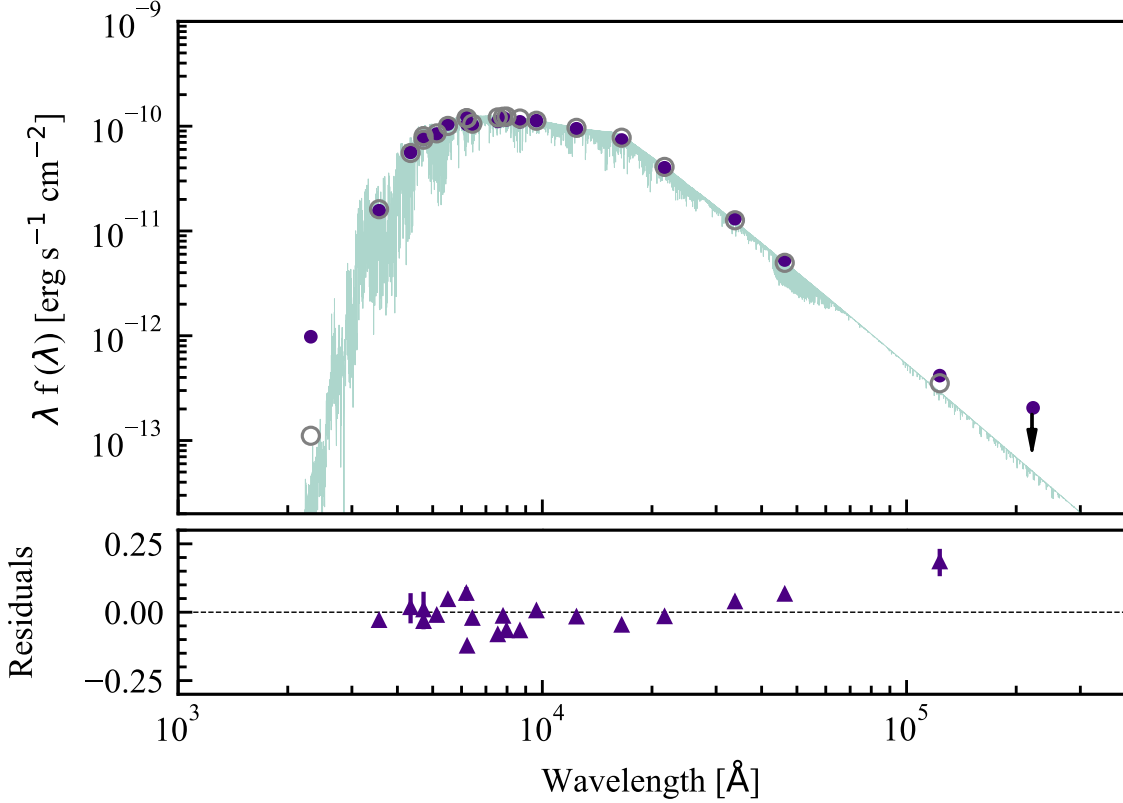


Figure 3. The spectral energy distribution of J1729+6529. The dark violet dots are the photometric data collected from *GALEX*, SDSS, APASS g and r bands, APASS GROUND JOHNSON B and V, Pan-STARRS, *Gaia*, *TESS*, 2MASS, and ALLWISE. The gray circles are the synthetic fluxes from the best-fitting theoretical spectral template. The black arrow indicates an upper limit of the WISE W4 band. The green curve is the best-fitting model. The lower panel shows the residuals calculated by the difference of the photometric and the synthetic fluxes divided by the synthetic fluxes. It should be noted that NUV, W3, and W4 were not involved in the SED fitting process. The residual value of NUV is too large to be displayed properly in the lower panel.

The companion in J1729+6529 ought to be a compact object for the following reasons. We calculate the mass M_2 of the invisible companion by using the mass function in Equation (4), where $M_1 = 0.81^{+0.07}_{-0.06} M_\odot$ from SED and mass function of $f(M_2) = 0.120 \pm 0.003 M_\odot$. The derived minimum value of M_2 is $0.63 M_\odot$, which corresponds to $i = 90^\circ$. Hence, the mass ratio of J1729+6529 is $q = M_2/M_1 \gtrsim 0.78$. In such case, the contribution of the companion to the optical band should be significant. However, CCFs indicate that the spectra of J1729+6529 are single-lined. Therefore, we conclude that the invisible companion is a compact object.

Furthermore, we focus on the absence of occultation in the light curves. We calculate the binary separation a by $G(M_1 + M_2)P_{\text{orb}}^2 = 4\pi^2 a^3$. We introduce the distance $\Delta d = R_1 + R_2 - a \cos i$, which is the geometric difference between the sum of the two stellar sizes and the projection of the binary separation. If $\Delta d > 0$ ($\Delta d < 0$), we expect eclipsing (non-eclipsing) light curves. The critical inclination angle (i_c) for $\Delta d = 0$ depends upon the masses and sizes of two stars and the period. Meanwhile, the mass of the secondary object can be calculated from the mass function (see Section 3.1) and the mass of the primary star (see Section 3.2) for each inclination angle. If the secondary object is a normal star, we can use the mass-radius relation of Eker et al. (2018) to derive R_2 . Hence, we derive a critical inclination angle ($i_c = 66^\circ$) for $\Delta d = 0$. If our binary is a late-type stellar companion, we expect that $i \lesssim i_c$ (i.e., $\Delta d < 0$) since the eclipsing signature is absent in the *TESS* light curve. The corresponding $M_2 \gtrsim 0.7 M_\odot$. In this case, the mass ratio increases to $q \gtrsim 0.86$, which means that the contribution of the companion should be even more significant. However, neither the spectra nor the photometry shows an excess component from the companion star. This further supports that the invisible companion is a compact object.

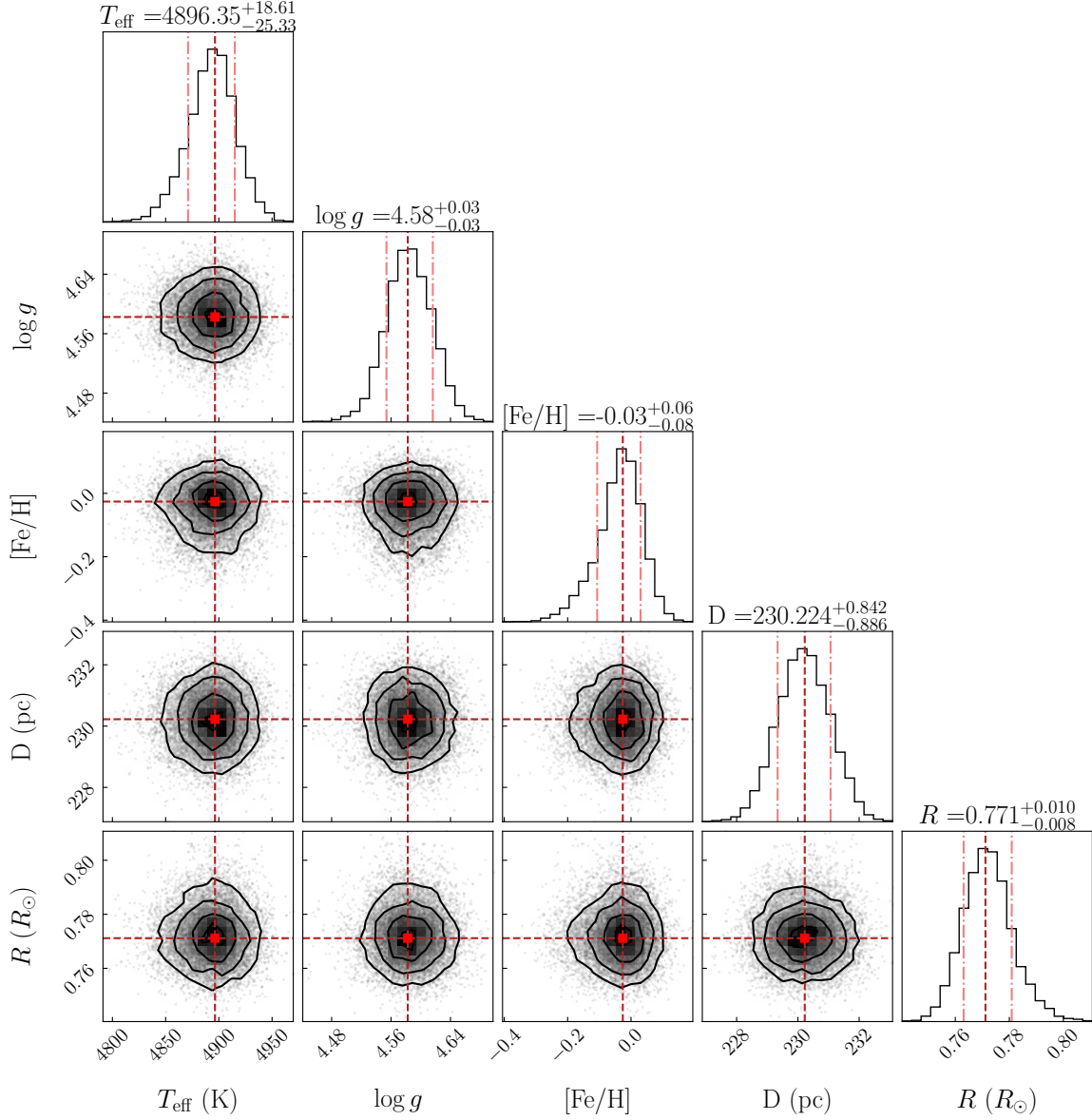


Figure 4. The distributions of the SED-fitting parameters. The black dots represent the nested MCMC samples, and the black curves are the contours with 1σ , 2σ , and 3σ probabilities, respectively. The red points are the best-fitted values.

3.4. Properties of the invisible companion

The compact object with the mass of $M_2 \gtrsim 0.63 M_\odot$ in J1729+6529 indicates that it can either be a WD or a NS, which mainly depends on the inclination i . Note that if the compact object is a NS with a typical mass $1.28 \pm 0.24 M_\odot$ (Özel et al. 2012), the inclination angle should be about 39^{+7}_{-5} degrees according to the mass function. In principle, one can constrain i by fitting the ellipsoidal variations to the high-cadence *TESS* light curves. In Figure 5, we plot the *TESS* light curves for sectors of 15-19, 21-22 and 24-26. It is clear that the light curves of J1729+6529 show unclear complex features. Possible origin of such complex features are due to the strong stellar activity. The impact factors on the light curves are variable, such as stellar surface differential rotation, rotation period, periodicity of active stars, shear, the number of spots, spot lifetime, and so on. More details can be referred to Basri et al. (2011); Basri & Nguyen (2018); Basri & Shah (2020); Walkowicz et al. (2013).

We argue that the compact object is a WD for the following reasons. It is evident that, compared with the best-fitting stellar spectral template, the SED has a clear NUV excess, which is well expected from a WD. Stellar chromospheric activity might also produce NUV emission and its strength is highly correlated with the H α emission (e.g., Jones &

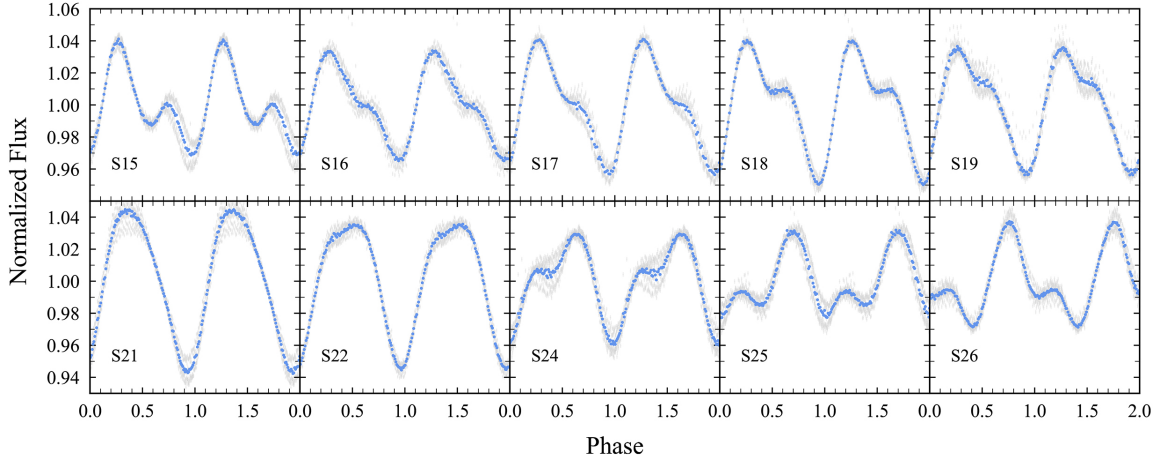


Figure 5. *TESS* light curves folded with the orbital period of 0.6003 days. The light curves in the phases of [1, 2] are the duplicates of those [0, 1] for clarity. The marker in each panel indicates the observed sector (e.g., S15 represents sector 15). The gray curves show the folded light curves, and the blue dots are the mean values over ten gray points.

West 2016; Linsky 2017). We did not detect the $H\alpha$ emission lines in most of the observed spectra of J1729+6529. Therefore, we argue that the NUV excess is dominated by the emission of a WD, although a small portion might be produced by the chromospheric emission of the visible star.

We constrain the WD’s effective temperature by comparing the NUV excess with the WD cooling models (Bergeron et al. 1995; Kowalski & Saumon 2006; Bergeron et al. 2011; Tremblay et al. 2011; Blouin et al. 2018; Bédard et al. 2020). The absolute NUV magnitude of J1729+6529 is $M_{\text{NUV}} = m_{\text{NUV}} - 5 \log(D) + 5 - A_{\text{NUV}} = 12.15$ mag, where m_{NUV} is the visual NUV magnitude from *GALEX*, D is the distance in pc, and $A_{\text{NUV}} = 0.25$ is the NUV extinction value derived by using the Milky Way Average Extinction Curve (Gordon et al. 2009). The synthetic colors for WDs are adopted from <http://www.astro.umontreal.ca/~bergeron/CoolingModels>. We investigate two cooling models of DA-type WDs with typical masses $M_2 = 0.60 M_\odot$ and $M_2 = 0.80 M_\odot$. These two masses correspond to orbital solutions with the inclination $i \approx 90^\circ$ and $i \approx 60^\circ$, respectively. As analyzed above, the absolute NUV magnitude of the WD should be $\gtrsim 12.15$ mag. Therefore, by looking up the cooling models, only WDs with $T_{\text{eff}}^{\text{WD}} \lesssim 12000$ K (for $M_2 = 0.60 M_\odot$) and $T_{\text{eff}}^{\text{WD}} \lesssim 13500$ K (for $M_2 = 0.80 M_\odot$) can satisfy the UV excess. The corresponding WD ages are $\gtrsim 0.39$ Gyr and $\gtrsim 0.45$ Gyr, respectively.

4. CONCLUSIONS AND DISCUSSION

J1729+6529 is a single-lined spectroscopic binary selected from the optical time-domain survey. We summarize our results as follows. First, we obtain the radial-velocity semi-amplitude $K = 124.4_{-1.1}^{+1.0}$ km s $^{-1}$ and orbital period $P_{\text{orb}} = 0.600303(6)$ days from the LAMOST and P200 spectra and the *TESS* high-cadence light curves. Second, we derive the mass $M_1 = 0.81_{-0.06}^{+0.07} M_\odot$ of the visible star via SED fitting. Third, we conclude that the unseen companion is a compact object owing to $M_2 \gtrsim 0.63 M_\odot$ and the single-lined spectra. Fourth, the compact object is likely to be a WD ($T_{\text{eff}}^{\text{WD}} \lesssim 12000 - 13500$ K) rather than a NS unless the inclination angle is small ($i \lesssim 40^\circ$). Our results suggest that the optical time-domain surveys, such as the joint of LAMOST and *TESS*, have great advantages in unveiling the faint WDs with bright companions (e.g., A, F, G, and K-type) or those hidden in the deep sky, and the method is also applicable to reveal other compact objects in binaries such as stellar-mass black holes (e.g., Yi et al. 2019).

In addition to optical and UV observations, we also searched for the possible X-ray counterparts of J1729+6529. The nearest detected X-ray source (2RXS J172901.3+652948) is in the ROSAT 2RXS Catalog of HEASARC (High Energy Astrophysics Science Archive Research Center)¹⁷, whose X-ray flux is $(3.08 \pm 0.54) \times 10^{-13}$ erg s $^{-1}$ cm $^{-2}$, and the corresponding luminosity is $L_X = (1.95 \pm 0.34) \times 10^{30}$ erg s $^{-1}$. The X-ray position is $6.4''$ away from the optical position of J1729+6529. Note that there is another brighter star which is $8.87''$ away from J1729+6529. Considering the angular resolution of ROSAT (is around $30''$), we cannot rule out the possibility that the ROSAT X-ray source is related to this nearby bright star. If the X-ray is indeed from J1729+6529, it may be emitted from the rapidly

¹⁷ <https://heasarc.gsfc.nasa.gov/cgi-bin/W3Browse/w3browse.pl>

rotating K star. The reason is that the ratio of X-ray luminosity to the bolometric luminosity $\log(L_X/L_{\text{bol}}) = -2.79$ is comparable to the rapidly rotating K stars (around -3 ; e.g., the sources of Speedy Mic and AB Dor in Table 5 of Singh et al. 1999).

For comparison, we collected known WDMS systems with A, F, G, K-type companions from previous works (e.g., Parsons et al. 2016; Rebassa-Mansergas et al. 2017; Ren et al. 2020, note that the cataclysmic variables are not considered for simplicity). The total number of such systems is around 3000, among which about 1000 systems have K-type companions ($3800 \text{ K} < T_{\text{eff}} < 5300 \text{ K}$). Most sources in the samples are WDMS candidates (except for 9 sources confirmed with HST spectra, Parsons et al. 2016), which were selected by the color index of FUV-NUV and the temperature of the visible stars, while the periods of these sources are often unknown. Well-identified WDMS binary with a bright companion (A, F, G, and K-type) is rare. We found only 11 such sources presented by Hernandez et al. (2021), of which the orbital periods and the masses were robustly measured. The three pink triangles in Figure 6 represent sources measured by Hernandez et al. (2021), and the green triangles represent other sources collected by Hernandez et al. (2021). By using the mass-radius relation in Eker et al. (2018) and the minimum orbital period (Equation (4) in Zheng et al. 2019), we plot a theoretical line of the minimum orbital periods $P_{\text{orb}}^{\text{min}}$ for given masses (black dashed line in Figure 6). Figure 6 shows that most A, F, G, and K-type sources have longer orbital periods compared to J1729+6529 (red star).

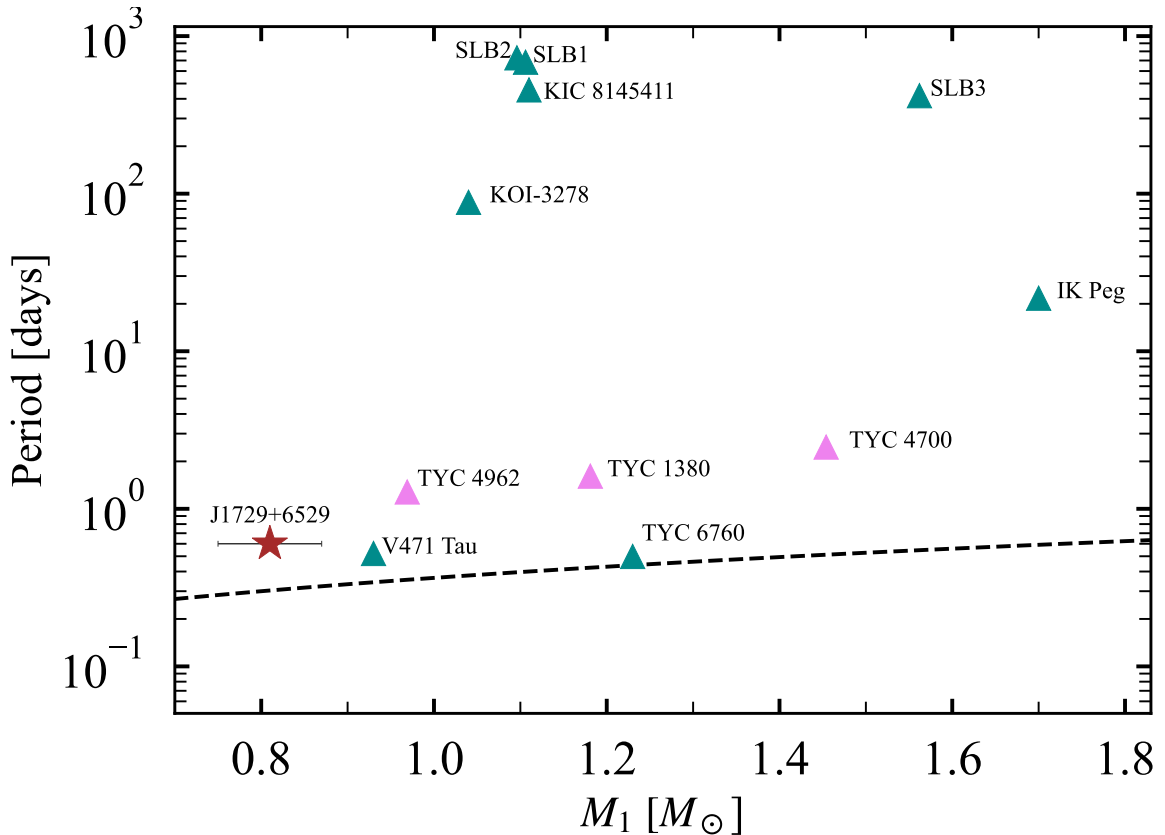


Figure 6. The pink triangles represent the sources with detailed parameters measured by Hernandez et al. (2021). The green triangles show the A, F, G, K-type WDMS collected by Hernandez et al. (2021). The red star denotes the source J1729+6529. The black dashed line shows the lower limit of the orbital period.

We thank the anonymous referee for constructive suggestions that improved the paper. This work was supported by the National Key R&D Program of China under grant 2021YFA1600401, and the National Natural Science Foundation of China under grants 11925301, 12033006, 11973002, 11988101, 11933004, 12103041, 12090044, 11833006, 12090042, U1831205, and U1938105. This work uses the data collected from multiple telescopes. Guoshoujing Telescope (the Large Sky Area Multi-Object Fiber Spectroscopic Telescope LAMOST) is a National Major Scientific Project built by the Chinese Academy of Sciences. Funding for the project has been provided by the National Development and Reform

Commission. LAMOST is operated and managed by the National Astronomical Observatories, Chinese Academy of Sciences. This paper includes data collected by the *TESS* mission, which is publicly available from the Mikulski Archive for Space Telescopes (MAST). This research uses data obtained through the Telescope Access Program (TAP), which has been funded by the TAP member institutes. This paper also includes public data collected by the NASA Galaxy Evolution Explorer (*GALEX*), SDSS, the Pan-STARRS1 Surveys (PS1), the Two Micron All Sky Survey (2MASS), the Wide-field Infrared Survey Explorer (WISE), the Zwicky Transient Facility (ZTF) project, ASAS-SN, the European Space Agency (ESA) mission *Gaia*, and the APASS database.

REFERENCES

- Abazajian, K. N., Adelman-McCarthy, J. K., Agüeros, M. A., et al. 2009, *ApJS*, 182, 543.
doi:10.1088/0067-0049/182/2/543
- Amôres, E. B., Jesus, R. M., Moitinho, A., et al. 2021, *MNRAS*, 508, 1788. doi:10.1093/mnras/stab2248
- Bar, I., Vreeswijk, P., Gal-Yam, A., et al. 2017, *ApJ*, 850, 34. doi:10.3847/1538-4357/aa91d4
- Basri, G., Walkowicz, L. M., Batalha, N., et al. 2011, *AJ*, 141, 20. doi:10.1088/0004-6256/141/1/20
- Basri, G. & Nguyen, H. T. 2018, *ApJ*, 863, 190.
doi:10.3847/1538-4357/aad3b6
- Basri, G. & Shah, R. 2020, *ApJ*, 901, 14.
doi:10.3847/1538-4357/abae5d
- Bédard, A., Bergeron, P., Brassard, P., et al. 2020, *ApJ*, 901, 93. doi:10.3847/1538-4357/abafbe
- Bergeron, P., Wesemael, F., & Beauchamp, A. 1995, *PASP*, 107, 1047. doi:10.1086/133661
- Bergeron, P., Wesemael, F., Dufour, P., et al. 2011, *ApJ*, 737, 28. doi:10.1088/0004-637X/737/1/28
- Blouin, S., Dufour, P., & Allard, N. F. 2018, *ApJ*, 863, 184.
doi:10.3847/1538-4357/aad4a9
- Chambers, K. C., Magnier, E. A., Metcalfe, N., et al. 2016, arXiv:1612.05560
- Cojocaru, R., Rebassa-Mansergas, A., Torres, S., et al. 2017, *MNRAS*, 470, 1442. doi:10.1093/mnras/stx1326
- Cui, X.-Q., Zhao, Y.-H., Chu, Y.-Q., et al. 2012, *Research in Astronomy and Astrophysics*, 12, 1197.
doi:10.1088/1674-4527/12/9/003
- Cutri, R. M., Wright, E. L., Conrow, T., et al. 2021, *VizieR Online Data Catalog*, II/328
- Eker, Z., Bakış, V., Bilir, S., et al. 2018, *MNRAS*, 479, 5491. doi:10.1093/mnras/sty1834
- Fontaine, G., Brassard, P., & Bergeron, P. 2001, *PASP*, 113, 409. doi:10.1086/319535
- Gaia Collaboration, Brown, A. G. A., Vallenari, A., et al. 2018, *A&A*, 616, A1. doi:10.1051/0004-6361/201833051
- Gaia Collaboration 2022, *VizieR Online Data Catalog*, I/355
- García-Berro, E., Ritossa, C., & Iben, I. 1997, *ApJ*, 485, 765. doi:10.1086/304444
- Gaskell, C. M. & Peterson, B. M. 1987, *ApJS*, 65, 1.
doi:10.1086/191216
- Gordon, K. D., Cartledge, S., & Clayton, G. C. 2009, *ApJ*, 705, 1320. doi:10.1088/0004-637X/705/2/1320
- Gu, W.-M., Mu, H.-J., Fu, J.-B., et al. 2019, *ApJL*, 872, L20. doi:10.3847/2041-8213/ab04f0
- Heller, R., Homeier, D., Dreizler, S., et al. 2009, *A&A*, 496, 191. doi:10.1051/0004-6361:200810632
- Henden, A. A., Welch, D. L., Terrell, D., et al. 2009, *AAS Meeting Abstracts*
- Henden, A. A., Terrell, D., Welch, D., et al. 2010, *AAS Meeting Abstracts*
- Henry, T. J. & McCarthy, D. W. 1993, *AJ*, 106, 773.
doi:10.1086/116685
- Hernandez, M. S., Schreiber, M. R., Parsons, S. G., et al. 2021, *MNRAS*, 501, 1677. doi:10.1093/mnras/staa3815
- Jones, D. O. & West, A. A. 2016, *ApJ*, 817, 1.
doi:10.3847/0004-637X/817/1/1
- Kepler, S. O., Pelisoli, I., Koester, D., et al. 2019, *MNRAS*, 486, 2169. doi:10.1093/mnras/stz960
- Kilic, M., Bergeron, P., Kosakowski, A., et al. 2020, *ApJ*, 898, 84. doi:10.3847/1538-4357/ab9b8d
- Kowalski, P. M. & Saumon, D. 2006, *ApJL*, 651, L137.
doi:10.1086/509723
- Li, L., Zhang, F., Han, Q., et al. 2014, *MNRAS*, 445, 1331.
doi:10.1093/mnras/stu1798
- Li, C.-qian., Shi, J.-rong., Yan, H.-liang., et al. 2021, *ApJS*, 256, 31. doi:10.3847/1538-4365/ac22a8
- Linsky, J. L. 2017, *ARA&A*, 55, 159.
doi:10.1146/annurev-astro-091916-055327
- Liu, C., Li, L., Zhang, F., et al. 2012, *MNRAS*, 424, 1841.
doi:10.1111/j.1365-2966.2012.21285.x
- Liu, C., Fu, J., Shi, J., et al. 2020, arXiv:2005.07210
- Liu, J., Zhang, H., Howard, A. W., et al. 2019, *Nature*, 575, 618. doi:10.1038/s41586-019-1766-2
- Lomb, N. R. 1976, *Ap&SS*, 39, 447.
doi:10.1007/BF00648343
- Magnier, E. A., Chambers, K. C., Flewelling, H. A., et al. 2020, *ApJS*, 251, 3. doi:10.3847/1538-4365/abb829

- Martin, D. C., Fanson, J., Schiminovich, D., et al. 2005, *ApJL*, 619, L1. doi:10.1086/426387
- Maxted, P. F. L., Gänsicke, B. T., Burleigh, M. R., et al. 2009, *MNRAS*, 400, 2012. doi:10.1111/j.1365-2966.2009.15594.x
- Merle, T., Van Eck, S., Jorissen, A., et al. 2017, *A&A*, 608, A95. doi:10.1051/0004-6361/201730442
- Morrissey, P., Conrow, T., Barlow, T. A., et al. 2007, *ApJS*, 173, 682. doi:10.1086/520512
- Mu, H.-J., Gu, W.-M., Yi, T., et al. 2022, *Science China Physics, Mechanics, and Astronomy*, 65, 229711. doi:10.1007/s11433-021-1809-8
- Oke, J. B. & Gunn, J. E. 1982, *PASP*, 94, 586. doi:10.1086/131027
- Özel, F., Psaltis, D., Narayan, R., et al. 2012, *ApJ*, 757, 55. doi:10.1088/0004-637X/757/1/55
- Parsons, S. G., Rebassa-Mansergas, A., Schreiber, M. R., et al. 2016, *MNRAS*, 463, 2125. doi:10.1093/mnras/stw2143
- Peterson, B. M., Wanders, I., Bertram, R., et al. 1998, *ApJ*, 501, 82. doi:10.1086/305813
- Price-Whelan, A. M., Hogg, D. W., Foreman-Mackey, D., et al. 2017, *ApJ*, 837, 20. doi:10.3847/1538-4357/aa5e50
- Raddi, R., Gentile Fusillo, N. P., Pala, A. F., et al. 2017, *MNRAS*, 472, 4173. doi:10.1093/mnras/stx2243
- Rebassa-Mansergas, A., Nebot Gómez-Morán, A., Schreiber, M. R., et al. 2012, *MNRAS*, 419, 806. doi:10.1111/j.1365-2966.2011.19923.x
- Rebassa-Mansergas, A., Ren, J. J., Parsons, S. G., et al. 2016, *MNRAS*, 458, 3808. doi:10.1093/mnras/stw554
- Rebassa-Mansergas, A., Ren, J. J., Irawati, P., et al. 2017, *MNRAS*, 472, 4193. doi:10.1093/mnras/stx2259
- Rebassa-Mansergas, A., Solano, E., Jiménez-Esteban, F. M., et al. 2021, *MNRAS*, 506, 5201. doi:10.1093/mnras/stab2039
- Ren, J.-J., Rebassa-Mansergas, A., Parsons, S. G., et al. 2018, *MNRAS*, 477, 4641. doi:10.1093/mnras/sty805
- Ren, J.-J., Raddi, R., Rebassa-Mansergas, A., et al. 2020, *ApJ*, 905, 38. doi:10.3847/1538-4357/abc017
- Ricker, G. R., Winn, J. N., Vanderspek, R., et al. 2015, *Journal of Astronomical Telescopes, Instruments, and Systems*, 1, 014003. doi:10.1117/1.JATIS.1.1.014003
- Scargle, J. D. 1981, *ApJS*, 45, 1. doi:10.1086/190706
- Silvestri, N. M., Hawley, S. L., West, A. A., et al. 2006, *AJ*, 131, 1674. doi:10.1086/499494
- Singh, K. P., Drake, S. A., Gotthelf, E. V., et al. 1999, *ApJ*, 512, 874. doi:10.1086/306788
- Skrutskie, M. F., Cutri, R. M., Stiening, R., et al. 2006, *AJ*, 131, 1163. doi:10.1086/498708
- Stassun, K. G., Oelkers, R. J., Pepper, J., et al. 2018, *AJ*, 156, 102. doi:10.3847/1538-3881/aad050
- Stassun, K. G., Oelkers, R. J., Paegert, M., et al. 2019, *AJ*, 158, 138. doi:10.3847/1538-3881/ab3467
- Taani, A. 2017, arXiv:1702.04419
- Ting, Y.-S., Conroy, C., Rix, H.-W., et al. 2019, *ApJ*, 879, 69. doi:10.3847/1538-4357/ab2331
- Tonry, J. & Davis, M. 1979, *AJ*, 84, 1511. doi:10.1086/112569
- Tremblay, P.-E., Bergeron, P., & Gianninas, A. 2011, *ApJ*, 730, 128. doi:10.1088/0004-637X/730/2/128
- Vines, J. I. & Jenkins, J. S. 2022, *MNRAS*. doi:10.1093/mnras/stac956
- Walkowicz, L. M., Basri, G., & Valenti, J. A. 2013, *ApJS*, 205, 17. doi:10.1088/0067-0049/205/2/17
- Waters, C. Z., Magnier, E. A., Price, P. A., et al. 2020, *ApJS*, 251, 4. doi:10.3847/1538-4365/abb82b
- Wesselius, P. R. & Koester, D. 1978, *A&A*, 70, 745
- Wiktorowicz, G., Lu, Y., Wyrzykowski, L., et al. 2020, *ApJ*, 905, 134. doi:10.3847/1538-4357/abc699
- Yang, F., Zhang, B., Long, R. J., et al. 2021, *ApJ*, 923, 226. doi:10.3847/1538-4357/ac31b3
- Yi, T., Sun, M., & Gu, W.-M. 2019, *ApJ*, 886, 97. doi:10.3847/1538-4357/ab4a75
- Zong, W., Fu, J.-N., De Cat, P., et al. 2018, *ApJS*, 238, 30. doi:10.3847/1538-4365/aadf81
- Zong, W., Fu, J.-N., De Cat, P., et al. 2020, *ApJS*, 251, 15. doi:10.3847/1538-4365/abbb2d
- Zhang, Z.-X., Zheng, L.-L., Gu, W.-M., et al. 2022, *ApJ*, 933, 193. doi:10.3847/1538-4357/ac75b6
- Zhao, G., Zhao, Y.-H., Chu, Y.-Q., et al. 2012, *Research in Astronomy and Astrophysics*, 12, 723. doi:10.1088/1674-4527/12/7/002
- Zheng, L.-L., Gu, W.-M., Yi, T., et al. 2019, *AJ*, 158, 179. doi:10.3847/1538-3881/ab449f
- Zverko, J., Žižňovský, J., Mikulášek, Z., et al. 2007, *Contributions of the Astronomical Observatory Skalnaté Pleso*, 37, 49

Table 3. The SED of J1729+6529

Telescope	Band	λ_{central}	magnitude	magnitude system	$\lambda f(\lambda)$
		\AA	<i>mag</i>		$\times 10^{-13} \text{erg s}^{-1} \text{cm}^{-2}$
(1)	(2)	(3)	(4)	(5)	(6)
GALEX	NUV	2313.89	19.211 ± 0.071	AB	9.81 ± 0.64
SDSS	u	3561.79	15.719 ± 0.005	AB	153.56 ± 0.71
	SDSS.g	4718.87	13.735 ± 0.074	AB	754.99 ± 51.46
	SDSS.r	6185.19	12.866 ± 0.026	AB	1276.00 ± 30.56
APASS	JOHNSON B	4347.53	14.223 ± 0.059	Vega	559.36 ± 30.40
	JOHNSON V	5504.67	13.168 ± 0.016	Vega	1062.18 ± 15.65
Pan-STARRS	g	4866.46	13.663 ± 0.013	AB	783.63 ± 9.38
	r	6214.62	13.078 ± 0.013	AB	1047.36 ± 12.54
	i	7544.57	12.793 ± 0.013	AB	1111.71 ± 13.31
	z	8679.48	12.642 ± 0.013	AB	1104.24 ± 13.22
	y	9633.26	12.506 ± 0.005	AB	1130.46 ± 5.21
	BP	5128.97	13.464 ± 0.005	Vega	854.84 ± 3.94
Gaia	G	6424.93	12.944 ± 0.001	Vega	1062.84 ± 0.98
	RP	7799.19	12.291 ± 0.003	Vega	1219.66 ± 3.37
TESS	red	7972.36	12.346 ± 0.007	Vega	1231.10 ± 7.94
	J	12408.38	11.516 ± 0.022	Vega	949.02 ± 19.23
2MASS	H	16513.66	11.004 ± 0.021	Vega	733.60 ± 14.19
	Ks	21655.84	10.889 ± 0.019	Vega	402.03 ± 7.04
	W1	33791.91	10.806 ± 0.023	Vega	132.54 ± 2.81
ALLWISE	W2	46292.96	10.816 ± 0.020	Vega	53.05 ± 0.98
	W3	123340.00	10.653 ± 0.046	Vega	4.44 ± 0.19
	W4	222530.00	> 9.328	Vega	< 2.06

Notes. The value of central wavelength can be accessed from the filter library of the PYPHOT^a. The magnitude systems are referred to the Filter Profile Service^b.

^a <https://mfouesneau.github.io/docs/pyphot/>

^b <http://svo2.cab.inta-csic.es/theory/fps/>